Nonlinear dynamics of a negative stiffness oscillator: experimental identification and model updating

EURODYN 2020
XI International Conference on Structural Dynamics
M. Papadrakakis, M. Fragiadakis, C. Papadimitriou (eds.)
Athens, Greece, 22–24 June 2020

NONLINEAR DYNAMICS OF A NEGATIVE STIFFNESS OSCILLATOR: EXPERIMENTAL IDENTIFICATION AND MODEL UPDATING

D. Anastasio, A. Fasana, L. Garibaldi, S. Marchesiello

Dipartimento di Ingegneria Meccanica ed Aerospaziale
Politecnico di Torino
Corso Duca degli Abruzzi, 24, 10129, Torino, Italy

Corresponding author: dario.anastasio@polito.it

Keywords: nonlinear dynamics, negative stiffness, double-well Duffing oscillator, experimental identification, model updating.

Abstract. *Systems exhibiting a negative stiffness region are often used as vibration isolators, due to their enhanced damping properties. The device tested in this paper is part of a damping system and it acts like an asymmetric double-well Duffing oscillator, with two stable and one unstable equilibrium positions. The range of motion can either be bounded around one stable position (in-well oscillations) or include all the three positions (cross-well oscillations). Depending on the input amplitude, the oscillator can exhibit linear and nonlinear dynamics, and chaotic motion as well. Due to its asymmetrical design, the two linearized systems associated to small-amplitude oscillations around one stable equilibrium position are different. In this work, the dynamical behavior of the system is first investigated in the case of linear and nonlinear in-well oscillations and then in the case of cross-well oscillations with chaotic motion. To accomplish this task, the device is mounted on a shaking table and it is driven through several excitation levels with both harmonic and random inputs. An experimental bifurcation tracking analysis is also carried out to understand the possible response scenarios. Afterwards, the nonlinear identification is performed using nonlinear subspace algorithms to extract the restoring force of the system. Eventually, the physically-based model of the device is updated to match the identified characteristics via genetic algorithms.*

1 INTRODUCTION

Devices and materials based on a negative stiffness behavior are very often used as vibration isolators due to their amplified damping properties [1,2]. In particular, in the case of engineering structures, examples can be found in automotive suspensions [3,4] or seismic isolation [5,6].

When the negative stiffness effect is coupled to a nonlinear polynomial stiffness contribution, the so-called double-well Duffing oscillator is obtained, whose dynamical properties have been extensively studied in the literature due to the wide kind of motions it can exhibit, ranging from linear to highly nonlinear and chaotic [7]. This oscillator exhibits two stable and one unstable equilibrium positions, and the oscillations can either be bounded around one stable point (in-well or intra-well small oscillations) or include all the three positions (cross-well or infra-well large oscillations). In both cases, periodic oscillations can evolve to steady in-well or cross-well chaotic motions under external excitation [8]. The occurrence of irregular motion, consisting of random-like crossings from oscillations around the two stable equilibrium positions, was first observed experimentally in 1971 [9] and the motion was called "snap-through". A comprehensive literature review about the Duffing equation can be found in [10].

In this work, a negative stiffness oscillator is studied and tested to derive a reliable nonlinear dynamical model. The dynamical properties of the oscillator are first investigated to uncover the possible kind of motions it can exhibit (in-well, cross-well, chaotic). To accomplish this tasks, the device is mounted on a shaking table and it is driven through several excitation levels with harmonic and random inputs. The experimental bifurcation diagram is estimated, together with the attractor surface in the case of chaotic motion.

Afterward, nonlinear system identification is performed to extract the model parameters directly from the measurements. The nonlinear subspace identification (NSI) method [11–14] is adopted to identify the nonlinear restoring force of the system using just one cross-well measurement obtained with random excitation. Eventually, a model updating procedure is implemented with genetic algorithms to refine the physically-based model based on the identified restoring force.

2 NEGATIVE STIFFNESS OSCILLATOR

The device under investigation consists in a U-shaped steel frame connected through rods to a central moving mass. The frame has the purpose to keep the rods under compression during their movement, exerting a compression force $p(\theta)$ depending on the rotation angle θ. A schematic representation of the device is depicted in Figure 1.

It is assumed that the inertia of the moving parts can be concentrated into one central point with mass m, comprising the mass of the central bushing and the equivalent inertia of the rods. The vertical movement of this point is described by the coordinate $y(t)$. The lower surface of the frame is attached to a shaking table, so that displacement $b(t)$ can be imposed to the structure. The free-body-diagram of mass m is depicted in Figure 1.

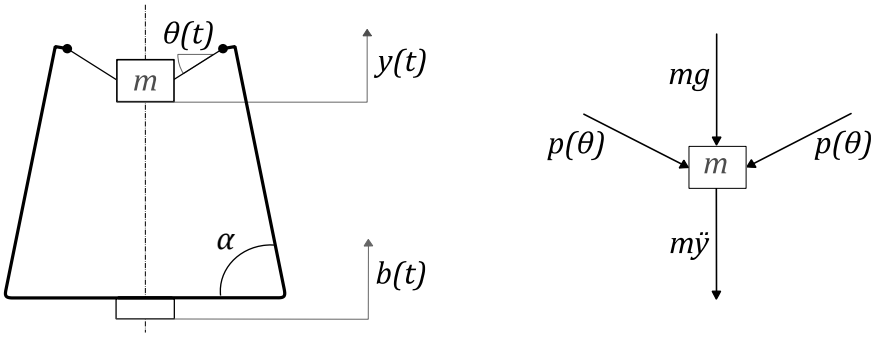

Figure 1: Schematic representation of the negative stiffness oscillator and free-body-diagram of *m*.

With $z(t) = y(t) - b(t)$, the equation of motion of the system in the variable z(t) can be written as

$$m\ddot{z} + k_3 z^3 + k_2 z^2 - k_1 z + k_0 = -m\ddot{b}, \tag{1}$$

where $k_0 = mg$ and the coefficients k_3, k_2, k_1 have to be experimentally estimated. Eq. (1) has the form of a negative-stiffness Duffing equation, and its restoring force K and elastic potential U can be defined as

$$K(z) = k_3 z^3 + k_2 z^2 - k_1 z + k_0, \tag{2}$$

$$U(z) = \frac{1}{4} k_3 z^4 + \frac{1}{3} k_2 z^3 - \frac{1}{2} k_1 z^2 + k_0 z. \tag{3}$$

A qualitative representation of the potential is shown in Figure 2, where its asymmetric double-well characteristic can be observed, together with the three equilibrium positions z^* obtained by setting $K(z^*) = 0$. Two out of three positions represent a stable equilibrium, namely z_-^* and z_+^*, while the central position z_0^* is an unstable point.

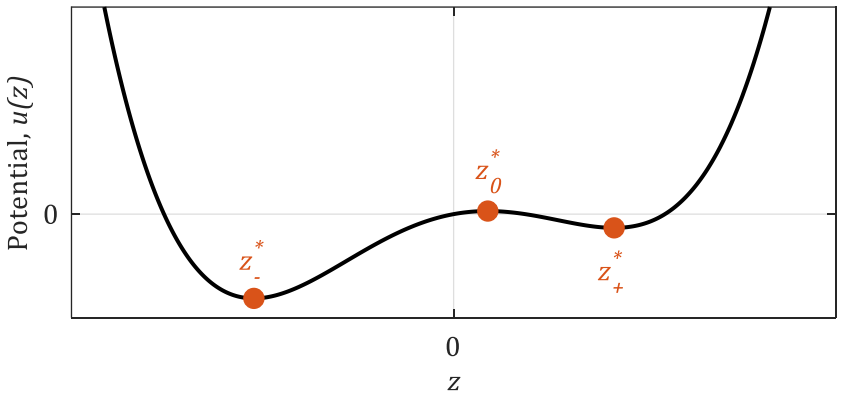

Figure 2: Potential $U(z)$. Orange dots: equilibrium positions.

The oscillations of the moving point are said to be *in-well* when the motion is bounded around one of the two stable equilibrium positions $z_{\pm}^{*}$. The associated linear natural frequency $\omega_{\pm}$ can be computed by

$$\omega_{\pm} = \sqrt{\frac{K'(z_{\pm}^{*})}{m}}, \tag{4}$$

$K'(z_{\pm}^{*})$ being the derivative of $K(z)$ computed in z_{-}^{*} or z_{+}^{*}.

3 EXPERIMENTAL CHARACTERIZATION

Two photos of the experimental setup corresponding to the two stable equilibrium positions are reported in Figure 3. The moving mass is instrumented with a laser vibrometer to measure its absolute displacement $y(t)$, whose zero position corresponds to the horizontal configuration of the rods ($\theta = 0$). The acceleration of the base $\ddot{b}(t)$ is also recorded through an accelerometer and the displacement $z(t)$ is computed as the difference between the laser measure $y(t)$ and the displacement of the base $b(t)$, obtained by integrating twice its measured acceleration.

The system is driven by harmonic inputs with fixed excitation frequency $\omega = 9 \cdot 2\pi$ rad/s and different amplitudes. The measured signals are sampled at 512 Hz. By applying this set of harmonic excitations, the so-called *bifurcation map* of the system can be built for a specific excitation frequency. The bifurcation map is a snapshot of the kind of steady-state solutions that can be obtained for a given excitation frequency when ranging over the excitation amplitude. Each point in the map represents the amplitude(s) of the steady-state solution for a specific value of the excitation amplitude. Indeed, the system can in principle exhibit super-harmonics of the exciting frequency (meaning frequency contents at $2\omega, 3\omega, 4\omega, \ldots$), sub-harmonics ($1/2\,\omega, 1/3\,\omega, 1/4\,\omega, \ldots$) or chaotic motion.

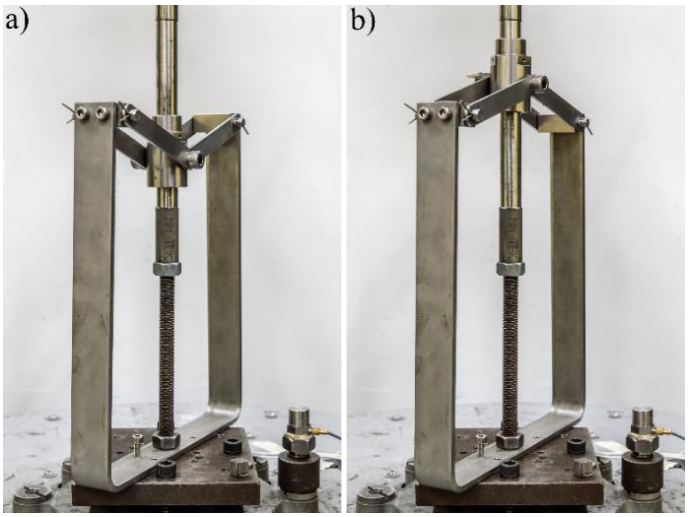

Figure 3: Photos of the experimental setup. a) Negative equilibrium position z_{-}^{*}; b) Positive equilibrium position z_{+}^{*}.

When building the bifurcation map on experimental time series, one should be able to detect the presence of super/sub-harmonics in order to correctly estimate the amplitude(s) of the response. This is done in this work automatically by performing a periodicity analysis of the measured displacement $z(t)$ over a certain number of periods of the input force. The algorithm seeks the number of periods that gives the *best* periodicity of the output signal:

- A *period-1* solution is gathered if the output is periodic with the input. The system in this case might respond with higher harmonics of the excitation frequency ω.
- A *period-2* solution is gathered if the output is periodic with twice the period of the input. The system in this case responds also with the sub-harmonic $1/2\ \omega$.
- A *period-4* solution is gathered if the output is periodic with four times the period of the input. The system in this case responds also with the sub-harmonics $1/2\ \omega, 1/4\ \omega$.
- ...

The experimental bifurcation map is depicted in Figure 4, where the cross-well region is highlighted in grey. Since the map is inferred from experimental measurements, it is not intended to be an exhaustive representation of all the possible bifurcations of the system, as it would be rather difficult to experimentally collect the huge number of points that would be required. Nevertheless, it gives useful information about the range of motions the system exhibits for different input amplitudes. In particular, a cascade of period doublings can be appreciated when the input amplitude is around $12 - 15\ \mathrm{m/s^2}$, especially when starting from the positive equilibrium position ($z_+^* = 0.023$ m).

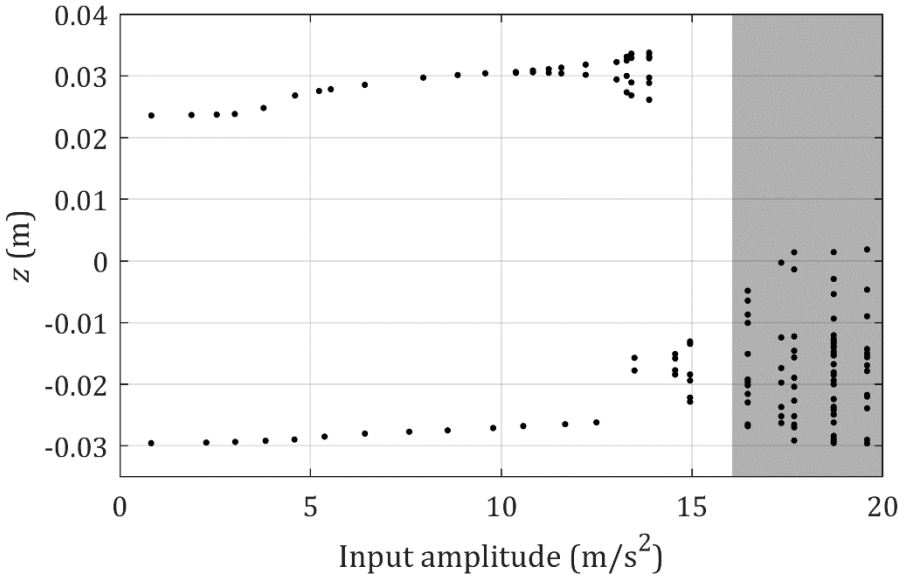

Figure 4: Experimental bifurcation map of the system. The chaotic region is highlighted in grey.

The time series and phase diagrams of some of the points of the bifurcation map are depicted in Figure 5. The selected phase diagrams correspond respectively to a period-1 solution, a period-2 solution, a period-4 solution and to a cross-well motion of the system. The latter in particular can be called *chaotic* in this context, as no periodic solution to a periodic input is retrieved, and this behavior lasts for the entire acquisition time (10 minutes).

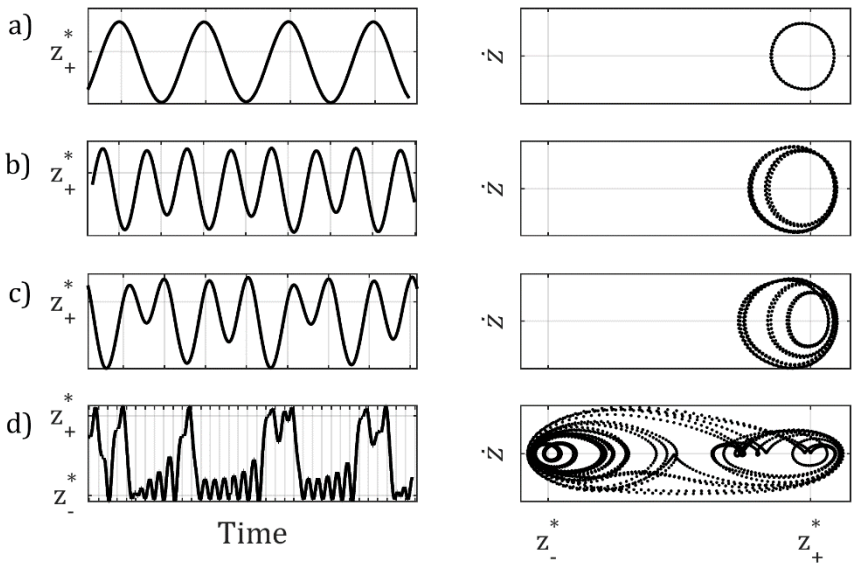

Figure 5: Time series and corresponding phase diagrams of selected measurements. a) Period-1 solution. b) Period-2 solution. c) Period-4 solution. d) Cross-well motion.

It should be recalled that no definition of *chaos* is universally accepted, and this is particularly true when experimental data is considered. The reason is that uncertainties and noise in the data acquisition may interfere with the extreme sensitivity to the initial conditions that characterizes chaotic systems.

The well-known LLE (largest Lyapunov exponent) [15] can be used to check whether the system is behaving chaotically or not: a positive sign means chaotic motion, while a negative sign is representative of a periodic orbit. Several methods exist to compute the LLE from experimental time series, and the one proposed in [16] is adopted here. Results are shown in Figure 6, where a positive sign is retrieved.

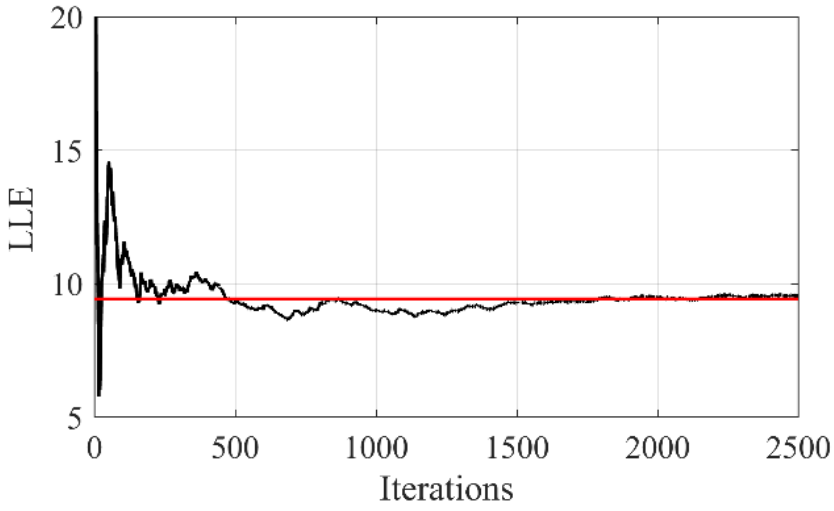

Figure 6: Estimation of the largest Lyapunov exponent. Red line: convergence mean value.

Eventually, the experimental Poincaré sections are computed for different phase synchronizations ϕ of the data with the forcing term [17]. The typical shape of a strange attractor is retrieved [8] and depicted in Figure 7a in a polar plot, while three of its sections are represented in Figure 7b,c,d.

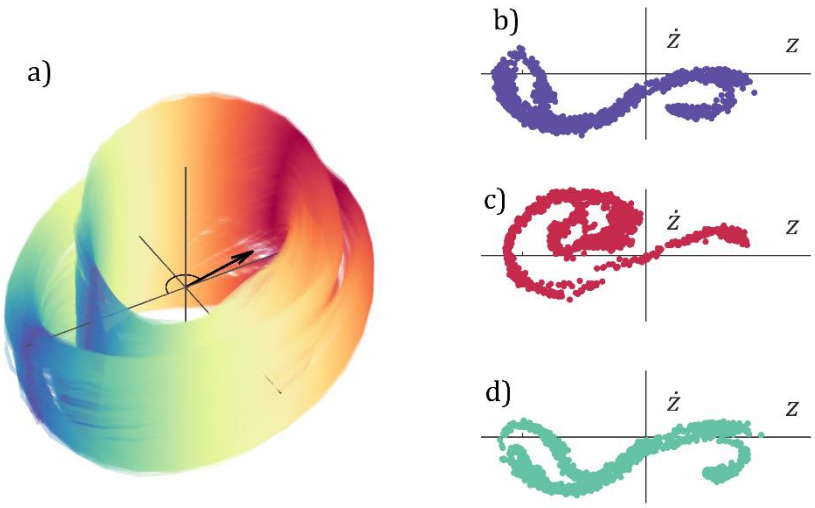

Figure 7: Experimental Poincaré sections. a) Polar representation of the attractor surface; b) Poincaré section, $\phi = 0°$; c) Poincaré section, $\phi = 170°$; d) Poincaré section, $\phi = 320°$.

4 IDENTIFICATION OF THE NONLINEAR RESTORING FORCE AND MODEL UPDATING

The nonlinear subspace identification (NSI) method is adopted in the following to identify the nonlinear state-space model of the system, with the final purpose of estimating its restoring force. NSI relies on the possibility of splitting the nonlinear equation of motion into an underlying-linear (and stable) system (ULS) and a nonlinear feedback. By looking at Eq. (1), this seems not to be possible for the considered system, as the negative linear stiffness creates an unstable ULS. Nevertheless, a workaround can be found by shifting the reference axis and considering the oscillations of the moving point around one *reference position*. This reference position is chosen as one of the two stable equilibrium points $z_{\pm}^{*}$, and it is generally referred to as z^{*}. A new variable $x(t)$ can therefore be defined as

$$x(t) = z(t) - z^{*}, \tag{5}$$

so as to write the equation of motion in the variable x

$$m\ddot{x} + K(x + z^{*}) = -m\ddot{b}, \tag{6}$$

with

$$K(x+z^*) = k_3x^3 + (k_2 + 3k_3z^*)x^2 + \left(3k_3{z^*}^2 + 2k_2z^* - k_1\right)x \\ = k_3x^3 + \tilde{k}_2x^2 + \tilde{k}_1x. \tag{7}$$

The new coefficients of the restoring force to be identified are therefore k_3, $\tilde{k}_2$ and $\tilde{k}_1$. Also, a nonlinear damping model of the kind $c^{nl}\dot{x}(t)|\dot{x}(t)|$ is sought by the method in addition to a linear viscous damping $c\dot{x}$, to account for the dissipation that comes with the relative motion between the moving point and the vertical steel guide.

Indeed, the ULS depends on the choice of the reference position z^*, therefore:

- When $z^* = z_-^*$ the modal parameters of the underlying-linear small oscillations around the *negative* equilibrium position can be estimated;
- When $z^* = z_+^*$ the modal parameters of the underlying-linear small oscillations around the *positive* equilibrium position can be estimated;

Consequently, two mutually exclusive ULSs can be obtained with NSI. For this reason, a single cross-well measurement under random excitation is fed to the NSI algorithm with two consecutive choices of the reference position: namely $z^* = z_-^*$ and $z^* = z_+^*$. The measurement is sampled at 512 Hz and lasts 300 s, with the last 60 s used for validation purposes.

A model order equal to 2 is chosen for the nonlinear state-space identification, the system being a single-degree-of-freedom system, and the corresponding modal parameters are listed in Table 1.

Reference position	Natural frequency (Hz)	Damping ratio (%)
z_-^*	11.41	11.2
z_+^*	9.19	20.3

Table 1: Modal parameters of the two underlying linear systems identified with NSI.

The validation of the identified model is carried out by simulating the output of the system $x^{SIM}(t)$ with the identified nonlinear state-space model, given the measured input. The simulated and the measured outputs are then compared to estimate the modeling error. Results are reported in Figure 8 in terms of simulated and measured time histories, in time and frequency domains. The statistical parameters of the residual between the measured output $x(t)$ and the simulated one $x^{SIM}(t)$ are listed in Table 2. Generally, the identified state-space model is capable of catching the cross-well motion with a very good accuracy, providing a percentage RMS deviation from the measurement of approximately 8%.

Once the identified model is validated, the coefficients of the nonlinear restoring force can be extracted [11–14], obtaining:

$$K(x+z^*) = k_3x^3 + \tilde{k}_2x^2 + \tilde{k}_1x \\ = 7.35 \cdot 10^5\, x^3 - 6.45 \cdot 10^3\, x^2 + 1.34 \cdot 10^3\, x. \tag{8}$$

The identified restoring force K and the corresponding potential U are depicted in Figure 9a,b. As for the nonlinear damping coefficient c^{nl}, a value of $-5\ \mathrm{Ns^2/m^2}$ is obtained. The total damping force $D(\dot{z}) = c\dot{z} + c^{nl}\dot{z}|\dot{z}|$ is depicted in Figure 9c.

Residual mean (mm)	Residual standard deviation (mm)
0.18	1

Table 2: Statistical parameters of the residual between measured and simulated outputs.

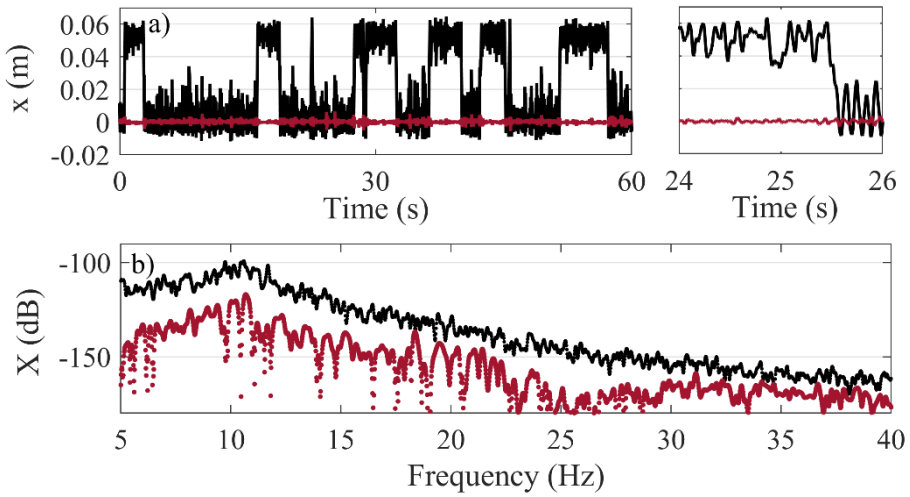

Figure 8: Validation of the nonlinear identification in the time domain (a) and frequency domain (power spectral density, b). Black line: measured output; red line: residual between simulated and measured output.

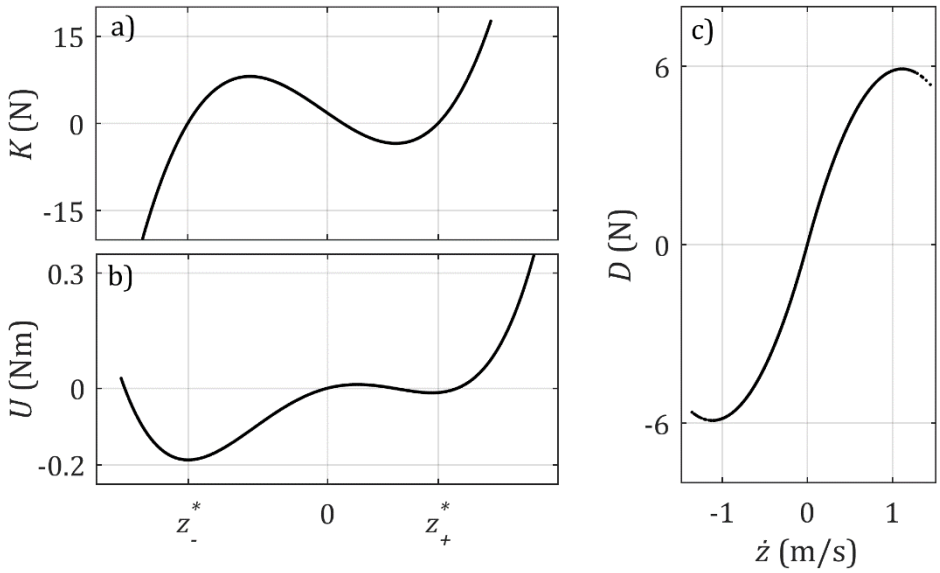

Figure 9: Estimation of the restoring force K (a), the corresponding potential U (b) and the damping force D (c).

4.1 Model updating

Once the parameters of the restoring force have been estimated from the experimental measurements, a comparison with the originally designed values is carried out to validate the model. A model updating procedure is implemented to adjust the physical parameters of the model and minimize the difference between simulated and identified behaviors. A genetic algorithm (GA) [18] is adopted to find the global optimum set of parameters. Genetic algorithms offer the chance to effectively update the model parameters, by exploring the range of feasible values in a smart and fast way. Also, crossover and mutation operators reduce the risk of falling into local minima [18]. The selected fitness function ϵ to be minimized is defined as the sum of two relative error functions ϵ_ω and ϵ_{z^*}. The function ϵ_ω is associated to the residuals on the positive and negative natural frequencies $\omega_\pm$, while ϵ_{z^*} is related to the residuals on the positive and negative equilibrium positions:

$$\epsilon_\omega = \mathrm{RMS}\left\{100\left|\frac{(\omega_-^{MOD} - \omega_-^{EST})}{\omega_-^{EST}}\right|, 100\left|\frac{(\omega_+^{MOD} - \omega_+^{EST})}{\omega_+^{EST}}\right|\right\}$$
$$\epsilon_{z^*} = \mathrm{RMS}\left\{100\left|\frac{(z_-^{*MOD} - z_-^{*EST})}{z_-^{*EST}}\right|, 100\left|\frac{(z_+^{*MOD} - z_+^{*EST})}{z_+^{*EST}}\right|\right\} \quad (9)$$
$$\epsilon = \epsilon_\omega + \epsilon_{z^*}$$

The superscripts *MOD* and *EST* stand respectively for "model" and "estimation". In particular, the estimated natural frequencies $\omega_\pm^{EST}$ are the ones listed in Table 1. The parameters to be optimized are the Young's modulus E of the frame, the frame angle α and the moving mass m. The values of the fitness function across the generations of GA are shown in Figure 10, while the final result is depicted in Figure 11.

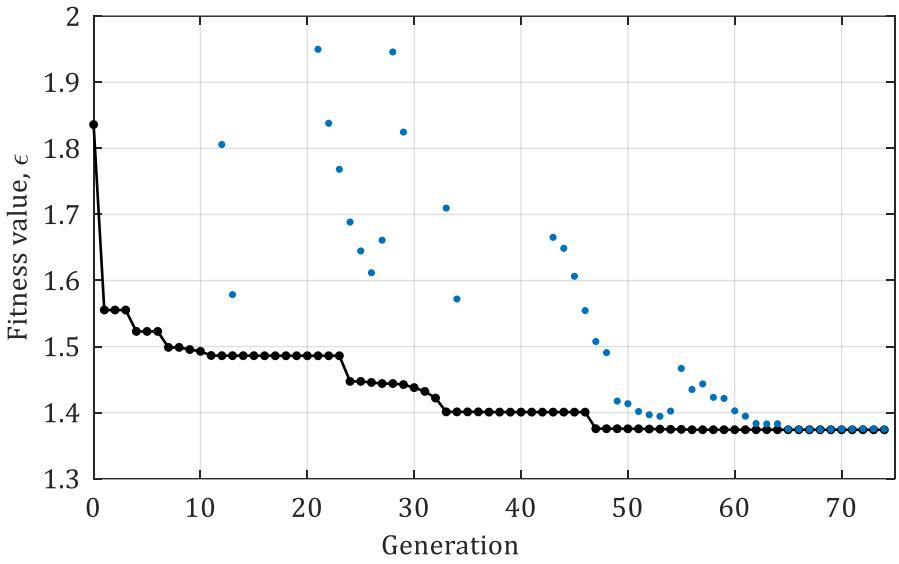

Figure 10: Values of the fitness function across the generations of GA. Black line: best fitness; blue dots: mean fitness values.

The optimization reduces the residual between the experimental characteristics and the model prediction, providing a good match between the final restoring force and potential curves, with a residual ϵ equal to 1.38%.

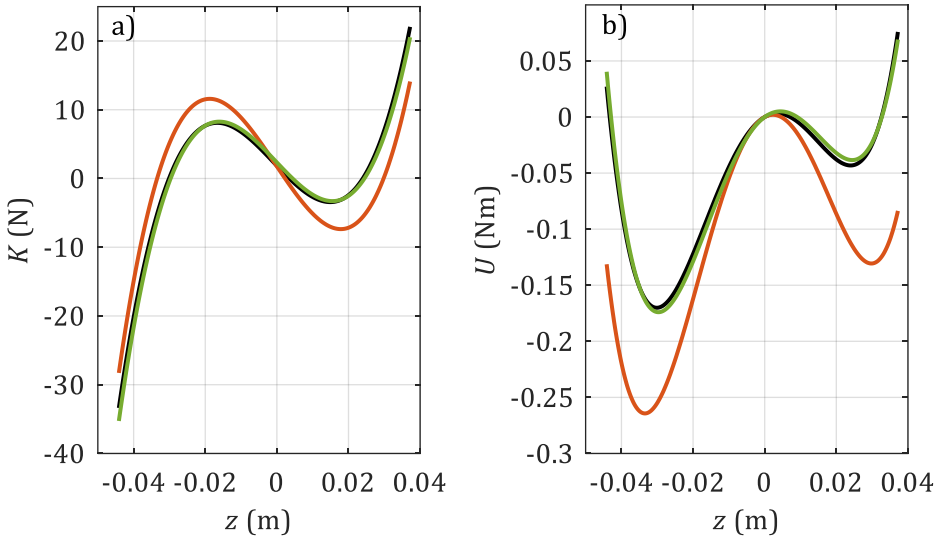

Figure 11: Results of the optimization in terms of restoring force in (a) and potential in (b). Black line: identified curves; orange line: starting values; green line: final values.

5 CONCLUSIONS

A negative stiffness oscillator has been characterized experimentally to exploit its dynamical behavior. A variety of different kind of motions can be obtained because of the bi-stable nature of the device, from in-well to cross-well oscillations, including chaotic motion. These dynamical behaviors have been confirmed by the experimental observations, obtained with harmonic inputs. The bifurcation map of the system has been estimated, together with the attractor surface in the case of chaotic motion. Eventually, the nonlinear restoring force of the system has been identified from the measured time series by applying the nonlinear subspace identification method, and the physically-based model of the device updated via genetic algorithm to match the experimental results.

REFERENCES

[1] R.S. Lakes, Extreme damping in composite materials with a negative stiffness phase, Physical Review Letters. 86 (2001) 2897–2900. https://doi.org/10.1103/PhysRevLett.86.2897.

[2] I. Antoniadis, D. Chronopoulos, V. Spitas, D. Koulocheris, Hyper-damping properties of a stiff and stable linear oscillator with a negative stiffness element, Journal of Sound and Vibration. 346 (2015) 37–52. https://doi.org/10.1016/j.jsv.2015.02.028.

[3] C.M. Lee, V.N. Goverdovskiy, A.I. Temnikov, Design of springs with “negative” stiffness to improve vehicle driver vibration isolation, Journal of Sound and Vibration. 302 (2007) 865–874. https://doi.org/10.1016/j.jsv.2006.12.024.

[4] T.D. Le, K.K. Ahn, A vibration isolation system in low frequency excitation region using negative stiffness structure for vehicle seat, Journal of Sound and Vibration. 330 (2011) 6311–6335. https://doi.org/10.1016/j.jsv.2011.07.039.

[5] H. Iemura, M.H. Pradono, Advances in the development of pseudo-negative-stiffness dampers for seismic response control, Structural Control and Health Monitoring. 16 (2009) 784–799. https://doi.org/10.1002/stc.345.

[6] A.A. Sarlis, D.T.R. Pasala, M.C. Constantinou, A.M. Reinhorn, S. Nagarajaiah, D.P. Taylor, Negative Stiffness Device for Seismic Protection of Structures, Journal of Structural Engineering. 139 (2013) 1124–1133. https://doi.org/10.1061/(ASCE)ST.1943-541X.0000616.

[7] D.W. Jordan, P. Smith, Nonlinear Ordinary Differential Equations: An Introduction for Scientists and Engineers, Fourth, Oxford University Press, New York, 2007.

[8] F.C. Moon, P.J. Holmes, A magnetoelastic strange attractor, Journal of Sound and Vibration. 65 (1979) 275–296. https://doi.org/10.1016/0022-460X(79)90520-0.

[9] W.-Y. Tseng, J. Dugundji, Nonlinear Vibrations of a Buckled Beam Under Harmonic Excitation, Journal of Applied Mechanics. 38 (1971) 467–476. https://doi.org/10.1115/1.3408799.

[10] I. Kovacic, M.J. Brennan, The Duffing Equation, John Wiley & Sons, Ltd, Chichester, UK, 2011. https://doi.org/10.1002/9780470977859.

[11] S. Marchesiello, L. Garibaldi, A time domain approach for identifying nonlinear vibrating structures by subspace methods, Mechanical Systems and Signal Processing. 22 (2008) 81–101. https://doi.org/10.1016/j.ymssp.2007.04.002.

[12] S. Marchesiello, A. Fasana, L. Garibaldi, Modal contributions and effects of spurious poles in nonlinear subspace identification, Mechanical Systems and Signal Processing. 74 (2016) 111–132. https://doi.org/10.1016/j.ymssp.2015.05.008.

[13] D. Anastasio, S. Marchesiello, Free-Decay Nonlinear System Identification via Mass-Change Scheme, Shock and Vibration. 2019 (2019). https://doi.org/10.1155/2019/1759198.

[14] D. Anastasio, S. Marchesiello, G. Kerschen, J.P. Noël, Experimental identification of distributed nonlinearities in the modal domain, Journal of Sound and Vibration. 458 (2019) 426–444. https://doi.org/10.1016/j.jsv.2019.07.005.

[15] S.H. Strogatz, Nonlinear Dynamics and Chaos, CRC Press, 1994. https://www.taylorfrancis.com/books/9780429492563.

[16] A. Wolf, J.B. Swift, H.L. Swinney, J.A. Vastano, Determining Lyapunov exponents from a time series, Physica D: Nonlinear Phenomena. 16 (1985) 285–317. https://doi.org/10.1016/0167-2789(85)90011-9.

[17] F.C. Moon, Experiments on Chaotic Motions of a Forced Nonlinear Oscillator: Strange Attractors, Journal of Applied Mechanics. 47 (1980) 638–644. https://doi.org/10.1115/1.3153746.

[18] K. Deb, Multi-Objective Optimization Using Evolutionary Algorithms, John Wiley & Sons, Inc., 2001.